JACS
JOURNAL OF THE AMERICAN CHEMICAL SOCIETY
Article
pubs.acs.org/JACS

Light Induced Carbon Dioxide Reduction by Water at Binuclear $ZrOCo^{II}$ Unit Coupled to Ir Oxide Nanocluster Catalyst

Wooyul Kim, Guangbi Yuan, Beth Anne McClure, and Heinz Frei*

Physical Biosciences Division, Lawrence Berkeley National Laboratory, University of California, Berkeley, California 94720, United States

Supporting Information

ABSTRACT: An all-inorganic polynuclear unit consisting of an oxo-bridged binuclear $ZrOCo^{II}$ group coupled to an iridium oxide nanocluster (IrO_x) was assembled on an SBA-15 silica mesopore surface. A photodeposition method was developed that affords coupling of the IrO_x water oxidation catalyst with the Co donor center. The approach consists of excitation of the $ZrOCo^{II}$ metal-to-metal charge-transfer (MMCT) chromophore with visible light in the presence of $[Ir(acac)_3]$ (acac: acetylacetonate) precursor followed by calcination under mild conditions, with each step monitored by optical and infrared spectroscopy. Illumination of the MMCT chromophore of the resulting $ZrOCo^{II}$–IrO_x units in the SBA-15 pores loaded with a mixture of $^{13}CO_2$ and H_2O vapor resulted in the formation of ^{13}CO and O_2 monitored by FT-IR and mass spectroscopy, respectively. Use of ^{18}O labeled water resulted in the formation of $^{18}O_2$ product. This is the first example of a closed photosynthetic cycle of carbon dioxide reduction by water using an all-inorganic polynuclear cluster featuring a molecularly defined light absorber. The observed activity implies successful competition of electron transfer between the IrO_x catalyst cluster and the transient oxidized Co donor center with back electron transfer of the ZrOCo light absorber, and is further aided by the instant desorption of the CO and O_2 product from the silica pores.

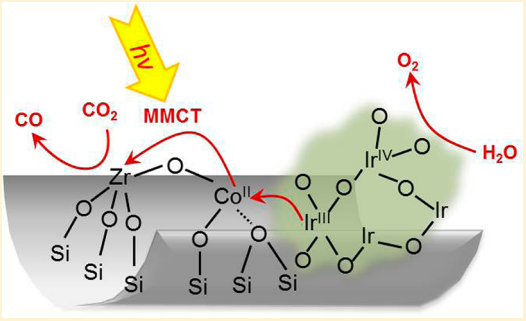

1. INTRODUCTION

Photochemical reduction of carbon dioxide by taking electrons from water molecules is among the most challenging scientific gaps of artificial photosynthesis, yet very attractive because of the possibility of generating a liquid solar fuel in a completely cyclic process. Substantial progress has been made in the past several years in the development of half reactions (subsystems) for visible light driven water oxidation and for carbon dioxide reduction by the direct coupling of molecular light absorbers to multielectron catalysts. Examples of light absorber–catalyst assemblies for water oxidation with visible light are Ru bipyridine sensitizer interacting with a benzimidazole-phenol mediator attached to an Ir oxide nanocatalyst,[1] or a Ru bipyridine chromophore coupled to molecular Mn cubane[2] or to a mononuclear Ru catalyst[3] embedded in a layer of Nafion. The same sensitizer was used for driving a Ru polyoxotungstate catalyst with the components coupled through strong electrostatic interactions,[4,5] or for activating a covalently attached single center Ru catalyst.[6] Another molecular assembly for water oxidation reported recently features a perylene dicarboximide chromophore linked to an organometallic Ir catalyst.[7] For visible light driven CO_2 reduction, chromophore–catalyst subsystems introduced thus far include an organo Ru or metalloporphyrin complex coupled via short hydrocarbon linkage or amide bridge to a Re bipyridine tricarbonyl catalyst.[8−11] Alternatively, nitrogen doped Ta_2O_5 nanoparticles were shown to serve as visible light absorbers for driving a Ru bipyridyl catalyst anchored on the particle surface.[12]

While there is a growing number of examples of molecular light absorbers driving a CO_2 reduction catalyst in the presence of an applied voltage or an energy-rich sacrificial donor (half reaction), examples do not yet exist where a molecular light absorber coupled to a CO_2 reduction catalyst uses electrons donated by H_2O molecules. Closing of the fuel producing cycle under visible light illumination in an energy bias-free (electrical of chemical) system has only been established for the reduction of protons to H_2 (overall water splitting), and primarily with semiconductor light absorbers. Examples are visible light water splitting at triple junction amorphous silicon,[13,14] III–V semiconducting materials,[15] WO_3 or Fe_2O_3 photoanode/dye sensitized[16] or $BiVO_4$/a-Si tandem cells,[17] and two-photon TiO_2/Si nanowire or n-WO_3/np$^+$Si microwire arrays.[18,19] GaN:ZnO materials functionalized with cocatalysts are an example of visible light induced overall water splitting using the semiconductor particle approach.[20] For direct photocatalytic CO_2 reduction by H_2O, existing systems are heterogeneous and based on wide bandgap semiconductor light absorbers like TiO_2, $SrTiO_3$, ZnO, SiC,[21,22] ZrO_2 with Cu cocatalyst,[23] layered perovskite $BaLa_4Ti_4O_{15}$ with Ag cocatalyst reported recently,[24] or engaging isolated Ti centers substituted in micro

Received: May 12, 2014
Published: July 17, 2014

   dx.doi.org/10.1021/ja504753g | J. Am. Chem. Soc. 2014, 136, 11034–11042

or mesoporous silicates.[25,26] However, in many reports, the formation of molecular oxygen product and, hence, closure of the photocatalytic cycle was not demonstrated, with notable exceptions.[23,24,27] Light absorption for all these materials is restricted to the UV region. Product analysis requires verification by isotopically labeled reactants to avoid effects caused by adventitious carbon residue that might be present in the solid photocatalyst material.[28] For the case of isolated Ti centers in mesoporous silica, CO and O_2 were shown to be the initial single photon products.[27] Reports are emerging of UV light driven CO_2 reduction by H_2O with enhanced selectivity to specific products. For example, a two-photon system consisting of an InP photocathode functionalized by an organo Ru complex coupled to TiO_2 particle to yield formate as the predominant product.[29] Also, MgO added to Pt loaded TiO_2 was shown to enhance selectivity toward methane product,[30] or a thin Nafion layer on Pd-deposited TiO_2 nanoparticles was found to promote methane and ethane production in aqueous suspension.[31]

Oxo-bridged, all-inorganic hetereobinuclear units covalently anchored on a silica surface possess metal-to-metal charge-transfer (MMCT) absorptions that reach deep into the visible region and are capable of driving a water oxidation catalyst, or reduce CO_2 to CO. About a dozen different units featuring Ti or Zr as acceptor and a first or second row transition metal as donor center have been developed in the past several years.[32−43] The wide choice of metals allows us to closely match the redox potential of donor or acceptor to the potential of the catalyst, which is important for converting a maximum fraction of the absorbed photon energy to chemical energy of products. The detailed structure of representative units such as $TiOMn^{II}$ and $ZrOCo^{II}$ on the surface of mesoporous silica supports has been determined by EXAFS spectroscopy.[42,43] The ability of most binuclear units to drive MMCT induced redox reactions is attributed to unusually long lifetimes of the excited charge transfer state.[41] Temperature dependent transient optical absorption spectroscopy of the excited state electron transfer processes in a $TiOMn^{II}$ unit revealed a slow back electron transfer time of 2.4 μs at room temperature, which is attributed to efficient ultrafast intersystem crossing to a lower spin state from the optically excited MMCT state.[44] Back electron transfer from the thermalized lower spin state to the high spin $TiOMn^{II}$ ground state requires intersystem crossing and is therefore slow, thus favoring charge transfer to a catalyst. For example, for a $TiOCr^{III}$ unit coupled to an Ir oxide nanocluster (2 nm) on the pore surface of mesoporous silica MCM-41, efficient visible light driven water oxidation was demonstrated (13% quantum efficiency at 458 nm).[36] The half reaction was conducted in liquid water, and persulfate was used as sacrificial acceptor. Units featuring Zr as acceptor linked to a Cu^{I} or a Co^{II} donor center allowed the direct reduction of CO_2 to CO upon MMCT excitation in mesoporous silica loaded with 1 atm of CO_2 gas. For the reduction at $ZrOCu^{I}$ units, no sacrificial donor was needed (Cu^{I} was stoichiometrically converted to Cu^{II}),[32] while the $ZrOCo^{II}$ unit required an amine sacrificial donor for the half reaction to produce CO and formate.[43]

In this paper, we report photodriven CO_2 reduction to CO at a heterobinuclear group by taking the electrons from water, thus demonstrating closure of the photosynthetic cycle at an all-inorganic polynuclear unit featuring a molecularly defined light absorber by recording reduced product and evolving oxygen for the first time. The system consists of a $ZrOCo^{II}$ group coupled to an Ir oxide nanocluster catalyst on the pore surface of mesoporous silica SBA-15. Photochemical activity was enabled by the development of a new photodeposition method for proper spatial arrangement of the catalyst cluster relative to the ZrOCo chromophore, and by suppressing back reaction by facile desorption of the CO and O_2 products from the photocatalytic site.

2. EXPERIMENTAL SECTION

2.1. Materials and Chemicals. The following reagents were used as received: Zirconocene dichloride ($[ZrCp_2Cl_2]$, >99%, Strem), anhydrous cobalt chloride (>98.0%, Fluka), triethylamine (TEA, >99%, Aldrich), anhydrous dichloromethane (99.8%, Aldrich), acetonitrile (>99.9%, Honeywell), ^{13}C-carbon dioxide (99% ^{13}C, Cambridge Isotope lab, Inc.), Pluronic P-123 (Aldrich), concentrated hydrochloric acid (37%, Aldrich), and $[Ir^{III}(acac)_3]$ (acac: $CH_3COCH{=}C(O^-)CH_3$, >97%, Aldrich). $[Ir^{III}(acacCl)_3]$ was synthesized according to literature procedure[45] and characterized by proton NMR by its characteristic signal at 2.26 ppm.[46] Solvents were dehydrated with 3 Å molecular sieves for acetonitrile and TEA, and 4 Å molecular sieves (Linde) for anhydrous methylene chloride and toluene. Molecular sieves (ca. 5 g/100 mL of solvent) were activated at 170 °C under vacuum for 24 h. Acetonitrile and TEA liquids were purged with nitrogen for 1 h and stored in a N_2 glovebox before use. Deionized ultrapure water (18 MΩ·cm) for CO_2 reduction experiments was placed in a Schlenk flask and degassed by three liquid nitrogen freeze−pump−thaw cycles. For ^{18}O labeling experiments, $H_2{}^{18}O$ (Icon, 97.6% ^{18}O) was used. Anhydrous cobalt chloride was heated at 120 °C under vacuum for 16 h before use to obtain an air-free sample. $[Ir^{III}(acac)_3]$ was kept under vacuum for 16 h before use, and $[ZrCp_2Cl_2]$ was kept in a N_2 glovebox to avoid water contamination.

2.2. Synthesis of ZrOCo-SBA-15. Mesoporous silica SBA-15 was prepared according to the method used in a previous report.[43] Binuclear ZrOCo units were assembled on the surface of SBA-15 mesopores by reaction of tetrahedral complex $[Co(II)(NCCH_3)_2Cl_2]$ on the nanopore surface of Zr-SBA-15.[34,35,43] Briefly, synthesis of the ZrOCo group on SBA-15 was achieved by first grafting tetrahedral Zr centers by conducting the known zirconocene dichloride precursor method in a dry N_2 box.[32,43,47] To remove the remaining organic ligand, calcination was conducted at 550 °C for 12 h, a procedure that is known to result in tripodally anchored ZrOH groups.[43,47,48] Covalent anchoring of Co followed the same method using as precursor the tetrahedral complex $[Co(II)(NCCH_3)_2Cl_2]$ in acetonitrile as reported previously.[34,35,43] Inductively coupled plasma (ICP) analysis for the determination of Zr, Co, and Ir content was conducted by ACTA Laboratories Inc. Subsequent removal of the remaining acetonitrile ligand by calcination at 350 °C (5 h) is known to result in anchored Co centers, the majority of which are oxo-bridged to a Zr center.[43] The detailed synthetic method and characterization of $ZrOCo^{II}$−SBA-15 including comprehensive spectroscopic characterization by powder X-ray diffraction (PXRD), extended X-ray absorption fine structure (EXAFS), FT-IR, FT-Raman, optical spectroscopy, and ICP analysis were described in our previous paper.[43] Small angle XRD data showing intact mesoporous structure after preparation of ZrOCo units are presented in Figure S1 in the Supporting Information. FT-IR spectra of SBA-15 and ZrOCo-SBA-15 are shown in Figure S2, which confirm the absence of impurities.

2.3. Photochemical Deposition of Ir Oxide Nanoclusters. The precursor $[Ir^{III}(acac)_3]$ for the assembly of Ir oxide nanoclusters (IrO_x) was loaded into SBA-15 pores by adding 50 mg of $ZrOCo^{II}$−SBA-15, dehydrated at 240 °C overnight under vacuum, to 90 μM (0.45 mg) of $[Ir^{III}(acac)_3]$ dissolved in toluene (10 mL). The solution was stirred for 1 h at room temperature in a dark environment inside a N_2 glove box. The powder was filtered, washed five times with 10 mL of toluene and dried in vacuum for 8 h. The as-synthesized powder (5 mg) was pressed with a KBr press (13 mm diameter) under ≤1 ton pressure for 5 s. The wafer was subsequently evacuated for 1 h in a homemade stainless steel optical cell equipped with a quartz window. For

dx.doi.org/10.1021/ja504753g | J. Am. Chem. Soc. 2014, 136, 11034−11042

photodeposition of Ir centers, the pellet loaded with $[Ir^{III}(acac)_3]$ was irradiated for 1 h at room temperature in vacuum using the 355 nm emission (127 mW cm^{-2}) of a pulsed Nd:YAG laser at 10 Hz (Continuum model Surelite III), or the 458 nm emission (460 mW cm^{-2}) of an Ar ion laser (Coherent model Innova) with the beam expanded to 1 in. diameter. The sample was calcined at 300 °C for 10 h under flow of O_2, resulting in the formation of a gray pellet containing $ZrOCo^{II}$ groups and Ir oxide nanoclusters, termed $ZrOCo^{II}$–IrO_x SBA-15. Typical IrO_x loading was estimated to be ca. 0.4 wt % (Ir/Si ratio) based on $[Ir^{III}(acac)_3]$ remaining in solution. The conversion of $[Ir^{III}(acac)_3]$ to $[Ir^{IV}(acac)_2]^{2+}$ was monitored by UV diffuse reflectance spectroscopy (UV-DRS, Shimadzu model UV-2100 spectrometer equipped with an integrating sphere model ISR-260) and by FT-IR spectroscopy (Bruker model IFS66 V equipped with LN_2 cooled MCT detector Kolmar model KMPV8-1-J2 with an 8 μm band gap). Transmission electron microscopic imaging was conducted at the TEAM0.5 instrument operated at 80 kV. Energy dispersive X-ray (EDX) data were collected at a TitanX instrument at the National Center for Electron Microscopy.

2.4. Photocatalysis. The $ZrOCo^{II}$–IrO_x SBA-15 wafer (5 mg) was placed in a home-built stainless infrared vacuum cell (volume 3.7 cm^3) equipped with CaF_2 windows and mounted in the FT-IR spectrometer for in situ monitoring of photocatalysis. After evacuation overnight at room temperature, H_2O and $^{13}CO_2$ gas were admitted to the infrared cell. After a 30 min dark period to confirm that no spectral changes occurred in the absence of light, laser photolysis (355 nm, 127 mW cm^{-2} at sample inside IR cell) was conducted at room temperature over a period of 5 h, and infrared spectra recorded at regular intervals. The spectral resolution was 0.25 cm^{-1}. To identify the origin of any carbon containing product, all experiments were carried out using isotopically labeled $^{13}CO_2$. Gas phase ^{12}CO and ^{13}CO can readily be differentiated by the characteristic ro-vibrational bands in the 2200–2000 cm^{-1} region. For monitoring of O_2 product, the gas phase of the cell was probed by a quadruple mass spectrometer (Pfeiffer model Omnistar 422).

3. RESULTS

3.1. Synthesis and Characterization of $ZrOCo^{II}$–IrO_x Unit. In a typical $ZrOCo^{II}$–SBA-15 sample (1.1 mol % Zr and 0.7 mol % Co), the majority of Co centers (>80%) are linked to a Zr center via an oxo bridge according to our previously reported EXAFS analysis. The selectivity is attributed to the preferential reaction of the ZrOH groups with $[Co^{II}(NCCH_3)_2Cl_2]$ precursor.[43] The optical diffuse reflectance spectrum of $ZrOCo^{II}$–SBA-15 has a distinct spin–orbit triplet of the $^4A_2(F) \rightarrow {}^4T_1(P)$ ligand field transition (500–700 nm) for tetrahedral Co^{II}, and a continuous $Zr^{IV}OCo^{II} \rightarrow Zr^{III}OCo^{III}$ metal-to-metal charge-transfer (MMCT) absorption tail from the near UV throughout the visible region to ca. 600 nm, as reported previously[43] and shown in Figure S3.

When exciting the ZrOCo MMCT absorption at 458 or 355 nm in the presence of loaded $[Ir(acac)_3]$, UV–vis DRS and FT-IR spectroscopy revealed conversion of $[Ir(acac)_3]$ on the SBA-15 pore surface to an oxidized $[Ir^{IV}(acac)_2]^{2+}$ group and free acetylacetone ligand. As shown in Figure 1a, spectra of $ZrOCo^{II}$–SBA-15 with loaded $[Ir(acac)_3]$ before (trace 1, black) and after 355 nm illumination for 1 h at 127 mW cm^{-2} (trace 2, red) indicate loss of $[Ir^{III}(acac)_3]$ and growth of $[Ir^{IV}(acac)_2]^{2+}$ along with free acac ligand. This conclusion is reached by comparison with the optical spectra of authentic samples of $[Ir^{III}(acac)_3]$, $[Ir^{IV}(acacCl)_2]^{2+}$ and free acac ligand in toluene solution, shown in Figure S4. Illumination results in decrease of the 317 nm peak of $[Ir^{III}(acac)_3]$ under growth of the (partially overlapping) band of free acac that absorbs at 299 nm (284 nm in the case of acac in toluene solution (Figure S4)). At the same time, the growth of $[Ir^{IV}(acac)_2]^{2+}$ is

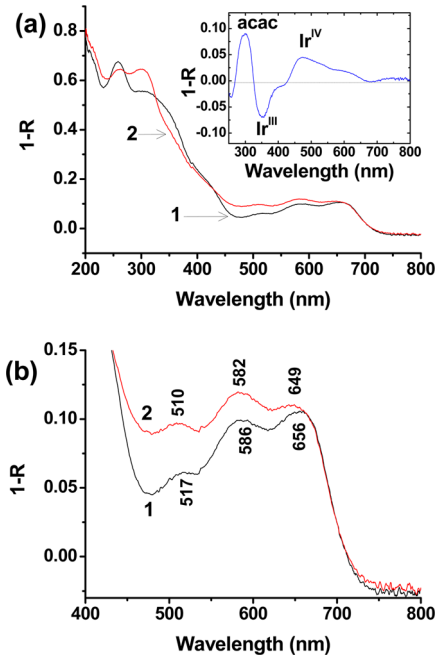

Figure 1. (a) UV–vis DRS of ZrOCo-SBA-15 loaded with $[Ir^{III}(acac)_3]$ before (trace 1, black) and after 1 h photodeposition (trace 2, red). Inset: Difference spectrum (2) − (1). Sample wafer was 5 mg, $[Ir(acac)_3]$ loading 0.045 mg, and 355 nm irradiation for 1 h (127 mW cm^{-2}). (b) Visible region of spectra (a) on an expanded scale for clarity. Samples were recorded under vacuum. Peak wavelengths were determined by Origin computer program, and an uncertainty of 1.0 nm was derived from the measurement of several independent samples.

manifested by absorbance increase at 440 nm and longer wavelengths (band extending to 650 nm), shown for clarity in Figure 1b on an expanded scale. The assignment of the Ir^{IV} absorption is based on a comparison of the spectra of the closely related authentic samples $[Ir^{III}(acacCl)_3]$ and $[Ir^{IV}(acacCl)_2]^{2+}$, and established spectral changes upon Ir^{III} to Ir^{IV} conversion as explained in the caption of Figure S4.[45,49] The spectral changes induced by the photodeposition are most clearly seen in the difference trace shown in the inset of Figure 1a. They were only observed for $[Ir^{III}(acac)_3]$ loaded into SBA-15 containing ZrOCo binuclear units, but not when the photodeposition process was attempted in single metal (Zr or Co) or neat SBA-15 (Figure S5). These findings provide strong evidence that the process is driven by light absorbed by the MMCT chromophore.

The shift of each of the three Co^{II} spin orbit peaks of the $ZrOCo^{II}$ unit to higher energy upon photodeposition (656, 586, and 517 nm before, 649, 582, and 510 nm after photodeposition, Figure 1b) is consistent with the formation of a Co^{II}–O–Ir^{IV} linkage because of the electron withdrawing effect of Ir^{IV} on the bridging O. Figure S6 describes control experiments which demonstrated that the blue shifts of 7, 4, and 7 nm for the three peaks are significant compared to shifts due to illumination of ZrOCo units or calcination for making Ir oxide clusters. This explanation is analogous to the effect of Zr^{IV} on the π donation to Co^{II} in the case of the $ZrOCo^{II}$ linkage reported previously.[43] Photodeposition was also achieved under visible light instead of 355 nm irradiation of the $ZrOCo^{II}$ MMCT transition using 458 nm laser emission of an Ar ion laser light (Figure S7). After calcination at 300 °C for 10 h under O_2 flow, the UV–vis bands of Ir-complexes

dx.doi.org/10.1021/ja504753g | J. Am. Chem. Soc. 2014, 136, 11034–11042

disappeared completely while the absorption of IrO_x grew in (Figure S8).[50]

The manifestation of the Ir photodeposition was corroborated by FT-IR spectroscopy. Infrared bands of $[Ir^{III}(acac)_3]$ loaded on $ZrOCo^{II}$–SBA-15, shown in trace 1 of Figure 2a

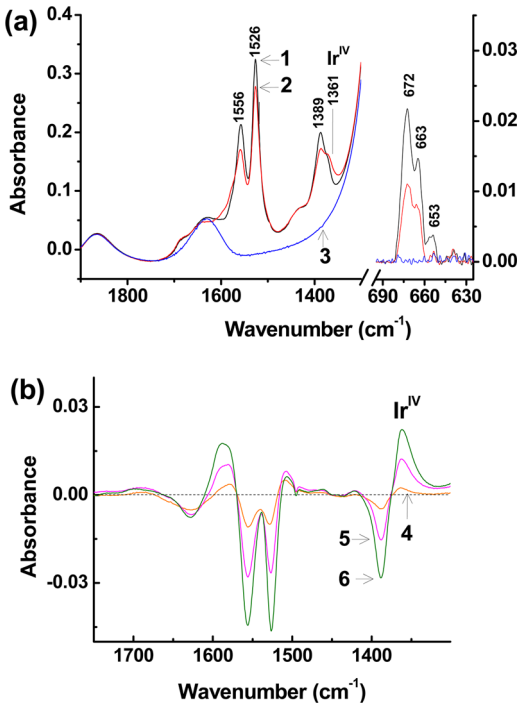

Figure 2. (a) FT-IR spectra of ZrOCo-SBA-15 loaded with $[Ir^{III}(acac)_3]$ before (trace 1, black) and after 1 h photodeposition with 355 nm light (127 mW cm^{-2}) (trace 2, red) in vacuum. The spectrum after calcination is shown as trace 3 (blue). (b) Difference FT-IR spectrum recorded before and after photodeposition for 10 min (trace 4, orange), 30 min (trace 5, red), and 60 min (trace 6, green). The 5 mg ZrOCo-SBA-15 pellet was loaded with 0.045 mg $[Ir^{III}(acac)_3]$.

agreed well with those of the solid complex dispersed in a KBr wafer (Figure S9),[45] indicating that after loading into ZrOCo-SBA-15 the structure of the complex remains intact. Upon photodeposition using 355 nm laser emission, decrease of $[Ir^{III}(acac)_3]$ bands at 1556, 1526, 1389, 672, 663, and 653 cm^{-1} was observed while absorptions grew in at 1690 (broad), 1587, 1507, and 1361 cm^{-1}. Among the latter, the first three bands are due to free acetylacetone/acetonate ligand[51] while the 1361 cm^{-1} peak, most clearly seen in the difference spectrum Figure 2b, is attributed to $[Ir^{IV}(acac)_2]^{2+}$. Infrared monitoring confirmed the results already established by UV–vis spectroscopy. FT-IR spectra obtained by photodeposition using visible light (458 nm) confirmed the results (Figure S10). Further, conversion of the Ir precursor to $[Ir^{IV}(acac)_2]^{2+}$, manifested by growth of the 1361 cm^{-1} band, is only observed in SBA-15 containing the $ZrOCo^{II}$ units, but not for single metal or bare SBA-15 samples (Figures S11; note that, in the absence of the ZrOCo chromophore, the $Ir^{III}(acac)_3$ complex itself is rendered photolabile by LMCT photoexcitation, resulting in a decrease of its bands and the formation of free acetylacetonate absorbing at 1367 cm^{-1}).

Upon calcination, the infrared peaks of the $[Ir(acac)_3]$ complex completely disappeared (trace 3 in Figure 2a), resulting in the formation of Ir oxide nanoclusters. Spectroscopic analysis and the observed photochemical activity (section 3.2 below) indicate that the ZrOCo binuclear units remain intact after growth of the IrO_x clusters. Far infrared spectra of the calcined $ZrOCo^{II}$–SBA-15 samples show no growth of Co–O modes of Co oxide clusters. Specifically, no growth is observed at 668 and 583 cm^{-1} characteristic for Co_3O_4 (Figure S12), which is the Co oxide structure expected to prevail under the applied calcination conditions.[34,43] UV–vis spectra (Figure S6) show that, after calcination, the Co^{II} centers remain tetrahedral with the first coordination sphere essentially unchanged (the spin orbit peaks are sensitive to coordination change). Furthermore, despite the high dispersion of $ZrOCo^{II}$–IrO_x units in the silica mesopores and the short penetration depth of soft X-rays into the SBA-15 particles, XPS measurements allowed us to confirm the oxidation state of Co^{2+}, Zr^{4+}, and Ir^{4+} upon calcination, as shown in Figure S13. Photochemical activation of CO_2 and reduction to CO is only observed for samples that start out with ZrOCo units followed by photodeposition of Ir and calcination to yield IrO_x clusters as shown in a series of FT-IR spectra in Figure S16 and described in section 3.2 below. No photoreduction is observed for IrO_x containing samples that have only one metal, Zr or Co. Because the presence of both Zr and Co is required for photochemical reaction to take place and the formation of a MMCT chromophore requires a covalent oxo bridge of the two metal centers as shown by our previous work, in particular, a study of the TiOCo unit,[34] the only explanation for the observed CO_2 photoreduction by $ZrOCo^{II}$ IrO_x samples we can conceive of is intact ZrOCo units after calcination. While the precise structural arrangement and whether covalent bonding between the Co and Ir center remains intact are not known, the photochemical results demonstrate that there is electron transfer communication between the Co donor center of the ZrOCo unit and the IrO_x cluster.

The analysis of high angle annular dark field (HAADF) images recorded in the STEM (scanning transmission electron microscopy) mode and energy dispersive X-ray (EDX) measurements confirmed the formation of uniform IrO_x nanoclusters in the channels of $ZrOCo^{II}$–SBA-15. The HAADF image of Figure 3a shows the mesoscale silica channels of a 0.4%(wt) Ir loaded $ZrOCo^{II}$–SBA-15 sample after photodeposition and calcination. The small bright spots are Ir oxide nanoclusters (example marked by dotted circle), which are absent in the same $ZrOCo^{II}$–SBA-15 sample before Ir loading, shown in Figure 3b. Inspection of close to 100 images revealed Ir oxide nanoclusters with an average diameter of 1.8 ± 0.1 nm (data points in the histogram shown in Figure S14 were analyzed using Digital Micrograph (Gatan Microscopy Suite) program). Assuming IrO_2 stoichiometry, a cluster of 1.8 nm diameter contains 96 Ir atoms based on the density of the crystal.[52] Hence, the ratio of ZrOCo chromophores and Ir oxide clusters is 10:1.

3.2. Photochemical Reduction of CO_2 by H_2O.

Illumination at 355 nm (127 mW cm^{-2}) of a pressed wafer of $ZrOCo^{II}$–SBA-15 containing Ir oxide nanoclusters (abbreviated $ZrOCo^{II}$–IrO_x SBA-15) loaded with a gas mixture of 760 Torr $^{13}CO_2$ and 100 mTorr H_2O resulted in the formation of ^{13}CO and O_2. Figure 4 shows the absorbance growth of the ro-vibrational bands of gas phase ^{13}CO in the region 2075 to 2050 cm^{-1} over a period of 5 h. No reproducible changes beyond the CO growth were observed in other spectral regions aside from an initial depletion at 1630 cm^{-1} of adsorbed H_2O due to consumption, and desorption upon start of photolysis (Figure

dx.doi.org/10.1021/ja504753g | J. Am. Chem. Soc. 2014, 136, 11034–11042

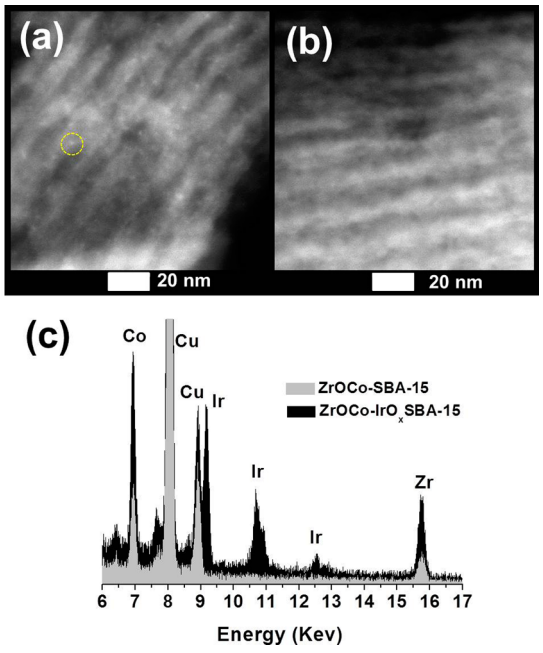

Figure 3. High angle annular dark field (HAADF) images of (a) ZrOCo^{II}–IrO$_x$ SBA-15 and (b) ZrOCo-SBA-15. (c) EDX measurement showing the exclusive presence of Zr, Co, and Ir (Cu is due to Cu grid).

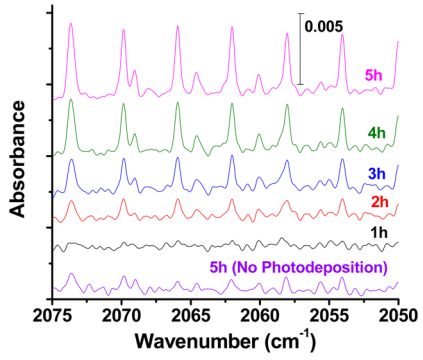

Figure 4. FT-IR monitoring of photoreduction of $^{13}CO_2$ by H_2O over ZrOCo–IrO$_x$ SBA-15 (5 mg pellet, 0.4 wt % IrO_2). Difference FT-IR spectrum (2075–2050 cm^{-1}) of gas phase ^{13}CO growth upon 355 nm irradiation (127 mW cm^{-2}) of ZrOCo^{II}–IrO$_x$ SBA-15 for 1 h (black), 2 h (red), 3 h (blue), 4 h (green), and 5 h (pink) and ZrOCo^{II}–IrO$_x$ (no photodeposition) SBA-15 for 5 h (violet) in the presence of 760 Torr $^{13}CO_2$ and 100 mTorr H_2O. Small bands at 2060.1, 2064.6, and 2069.1 are due to ^{12}CO generated by the reaction of O split off from $^{13}CO_2$ with adventitious carboneous residue present in SBA-15, as described in previous work.[27]

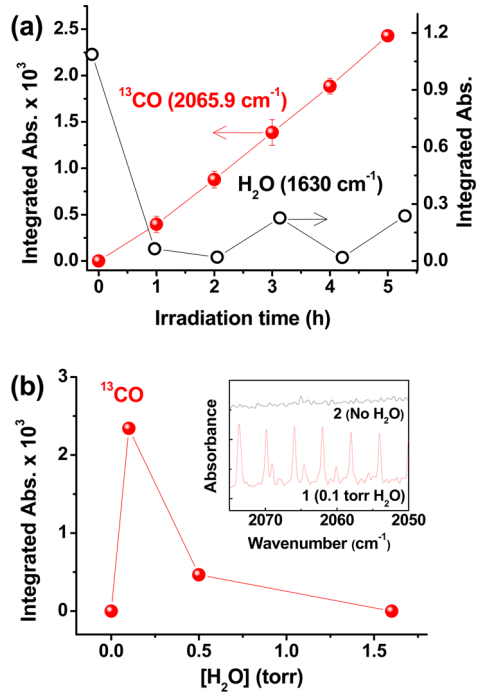

Figure 5. (a) Growth kinetics of ^{13}CO (at 2065.9 cm^{-1} band) and the behavior of H_2O adsorbed on ZrOCo–IrO$_x$ SBA-15 (intensity of 1630 cm^{-1} band). The yield of ^{13}CO product after 5 h photolysis is 43.6 nmol corresponding to 46 catalytic turnovers at IrOCo–IrO$_x$ sites. The error bars of the ^{13}CO growth represent the statistical uncertainty of four experiments with samples from fresh batches. (b) Effect of added H_2O concentration (initially indicated by the absorbance of the 1630 cm^{-1} H_2O mode) on the production of ^{13}CO upon 355 nm irradiation of ZrOCo–IrO$_x$ SBA-15 for 5 h photolysis. Inset: Difference FT-IR spectrum (2075–2050 cm^{-1}) of gas phase ^{13}CO growth for 5 h of ZrOCo^{II}–IrO$_x$ SBA-15 in the presence (trace 1, red) and absence (trace 2, black) of H_2O upon 355 nm irradiation (127 mW cm^{-2}).

5a; for completeness, mid-infrared spectra of several photolysis experiments are shown in Figure S15). As shown in Figure 5a, the growth of ^{13}CO product is close to linear with time. The slight deviation from a perfect straight line is consistent with the fact that the natural line width of a ro-vibrational CO band is significantly smaller (0.03 cm^{-1}) than the spectral resolution of 0.25 cm^{-1} of the FT-IR spectrometer. Taking into account the systematic error caused by the limited spectral resolution, the total amount of ^{13}CO produced over a 5 h photolysis period was determined as 43.6 nmol, which corresponds to 46 turnovers per ZrOCo–IrO$_x$ catalytic site.

A series of control experiments gave insight into key properties of this photosynthetic system consisting of a ZrOCo charge transfer unit coupled to an IrO$_x$ nanocluster catalyst. Of foremost interest is the observation that, in the absence of H_2O, no ^{13}CO growth (and no O_2 growth, see next paragraph) is observed, as shown in the water concentration plot of Figure 5b. The result implies that electrons generated by the oxidation of water enable the photoreduction of carbon dioxide. Furthermore, if the Ir oxide nanocluster catalysts are prepared in the ZrOCo-SBA-15 material without applying the photodeposition step, that is, by direct calcination of ZrOCo-SBA-15 loaded with [Ir^{III}(acac)$_3$], photochemical ^{13}CO product growth is negligible, as shown in Figure 4, bottom trace (violet). This finding strongly suggests that the photodeposition method indeed results in the proper spatial positioning of the Ir oxide nanocluster close to the Co donor center. Random formation of oxide clusters in the SBA-15 mesoscale channels does not lead to adequate coupling of Co donor centers with the nanocluster for water oxidation.

As the CO product increases over a period of 5 h of photolysis, the level of adsorbed H_2O as monitored by the bending mode at 1630 cm^{-1} (Figure 5a, black curve) remains unchanged with photolysis time following the initial loss at the onset of illumination (mainly caused by the minor heating (about 2°) by the laser emission). The finding indicates that

dx.doi.org/10.1021/ja504753g | J. Am. Chem. Soc. 2014, 136, 11034–11042

adsorbed water is continuously replenished from the vapor phase.

Additional control experiments summarized in Figure S16 confirm that no photoreduction of carbon dioxide occurs in the absence of IrO_x clusters, in the absence of the ZrOCo chromophore, or when leaving a photoactive $ZrOCo^{II}$–IrO_x SBA-15 sample in the dark.

The photochemical production of ^{13}CO by the $ZrOCo^{II}$–IrO_x SBA-15 system was investigated by independently varying H_2O (Figure 5b) and IrO_x concentrations (Figure S17). The CO production rate in the presence of H_2O (at 0.1 Torr) and IrO_x (at 0.1 mol % or 0.4 wt % with respect to silica) exhibits a maximum beyond which the rates decreased with increasing the concentration of each component. The finding that the CO_2 photoreduction yield decreases with increasing IrO_x loading is consistent with the growing inner filter effect, as shown in Figure S17b.

To further confirm the role of water as an electron donor, the production of O_2 (m/z = 32) was analyzed by mass spectroscopy. Figure 6a trace 1 shows the O_2 signal observed when injecting into the mass spectrometer the gas content of the sample cell after 5 h illumination of a $ZrOCo^{II}$–IrO_x SBA-15 wafer in the presence of $^{13}CO_2$ (760 Torr) and H_2O (0.1 Torr). No O_2 signal outside uncertainty (at m/z = 32) was detected when repeating the same experiment in the absence of H_2O (Figure 6a, trace 2). Furthermore, no O_2 was produced under otherwise identical experimental conditions without illumination (Figure 6a, trace 3). When conducting identical photolysis experiments with $H_2{}^{18}O$ using $^{13}C^{16}O_2$ as coreactant, $^{18}O_2$ (m/z = 36) was detected (Figure 6b, trace 4), thus further confirming that water is oxidized to O_2. We conclude from these findings that the generation of both CO and O_2 requires photooxidation of H_2O at $ZrOCo^{II}$–IrO_x units induced by MMCT excitation of the ZrOCo chromophore.

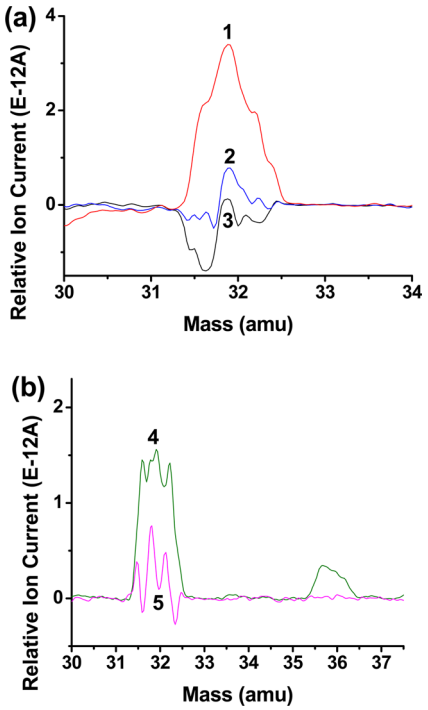

Figure 6. (a) Mass spectrum of O_2 produced after 355 nm irradiation of $ZrOCo$–IrO_x SBA-15 for 5 h with $^{13}CO_2$ and H_2O (trace 1, red). The control experiments were conducted under exactly the same condition without H_2O (trace 2, blue) or without photolysis (trace 3, black). Traces represent the average of three experiments, each conducted with a fresh $ZrOCo$–IrO_x SBA-15 pellet. Experimental conditions were [$ZrOCo$–IrO_x SBA-15] = 0.5 mg/pellet (with 0.4 wt % IrO_2), [$^{13}CO_2$] = 760 Torr, [H_2O] = 0.1 Torr, illumination with 355 nm emission of a pulsed Nd:YAG laser at 10 Hz (127 mW cm^{-2}). (b) Mass spectrum of $^{18}O_2$ and $^{16}O_2$ produced under identical experimental conditions using $^{13}CO_2$ and $H_2{}^{18}O$ (trace 4, green). Control experiment of identical sample but without photolysis (trace 5, purple). Traces represent the average of two experiments, each conducted with a fresh $ZrOCo$–IrO_x SBA-15 pellet.

4. DISCUSSION

The observed photoreduction of CO_2 by 355 nm excitation of $ZrOCo^{II}$–IrO_x units using H_2O as electron source is consistent with our previous observations on the corresponding oxidation and reduction half reactions. Water oxidation was observed in aqueous suspension upon MMCT excitation at 458 nm of $TiOCr^{III}$ units coupled to an IrO_x nanocluster catalyst. The units were anchored in mesoporous AlMCM-41 and $Na_2S_2O_8$ used as sacrificial electron acceptor. For this photocatalytic assembly, proper spatial arrangement of the IrO_x cluster adjacent to the Cr^{III} donor center was achieved by spontaneous (dark) reaction of [$Ir^{III}(acac)_3$] with TiOCr units, with the donor center in the Cr^{V} oxidation state.[36] Furthermore, studies of water oxidation at nanosized IrO_x clusters by an organometallic visible light sensitizer, $[Ru(bpy)_3]^{2+}$ ($Ru^{3+/2+}$ redox potential: 1.24 V), showed that the overpotential for driving the catalyst is at most 350 mV, or 8.5 kcal mol^{-1} (pH 6).[53−55] Electrochemical measurements at 2 nm IrO_2 particles were found to yield overpotentials of 250 mV (5.8 kcal mol^{-1} at 0.5 mA cm^{-2}),[56,57] and even lower values of 190 mV (at 1 mA cm^{-2}) were reported very recently for amorphous Ir oxide films.[58] Regarding the CO_2 reduction half reaction, CO_2 splitting was demonstrated previously at a different Zr containing heterobinuclear unit, namely, $ZrOCu^{I}$.[32] The reaction was induced in $ZrOCu^{I}$–MCM-41 mesoporous silica loaded with 760 Torr CO_2 gas by $Zr^{IV}OCu^{I} \rightarrow Zr^{III}OCu^{II}$ excitation with 355 nm photons and proceeded in the absence of any sacrificial electron donor under stoichiometric oxidation of Cu^{I} to Cu^{II}. H_2O was the coproduct of CO.[32] Although CO is trapped inside the mesoscale silica channels because of strong coordination with Cu^{I} centers, this example constitutes a precedent for a MMCT unit with Zr acceptor capable of reducing CO_2 to CO without involving a sacrificial acceptor.

The observed conversion of CO_2 to CO and O_2 by taking the electrons from H_2O upon excitation of the $ZrOCo^{II}$–IrO_x unit with a 355 nm photon is consistent with the energetics of the reaction. The free energy of the reaction $CO_2 \rightarrow CO + 1/2O_2$ (gas phase) is 62 kcal mol^{-1}.[27,59] Given the energy of 355 nm photons (80.5 kcal mol^{-1}), the available energy for surpassing the barriers for the multielectron transfer processes of water oxidation to O_2 and CO_2 reduction to CO is 18.5 kcal mol^{-1}. This value must be considered as an upper limit because of likely vibronic/electronic relaxation within the ZrOCo unit prior to charge transfer to the IrO_x catalyst or electron transfer to CO_2. However, the estimated activation energy for driving water oxidation catalysis with the IrO_x cluster is just a few kcal mol^{-1} according to the discussion of the previous paragraph. A similarly accurate estimate for the activation of CO_2 by a Zr^{III} center is not available. However, with reduction of CO_2 to CO at transient Zr^{III} in another endoergic MMCT-induced reaction demonstrated previously ($Zr^{IV}OCu^{I}$ converted to $Zr^{IV}OCu^{II}$),[32]

dx.doi.org/10.1021/ja504753g | J. Am. Chem. Soc. 2014, 136, 11034−11042

the observed CO_2 splitting at $ZrOCo^{II}$–IrO_x units with 355 nm photons under electron donation by H_2O is anticipated.

The quantum efficiency (QE) of CO_2 reduction to CO by H_2O is estimated according to

$$QE = \frac{2N_{CO}}{N_{incident\_photons}\alpha\beta}$$

where N_{CO} is the number of CO produced per second (1.45×10^{12} s^{-1}), $N_{incident\_photons}$ is the number of 355 nm photons per second (2.3×10^{17} s^{-1}), α is the fraction light absorbed by ZrOCo in SBA-15 at 355 nm (0.065), and β is the fraction of ZrOCo which has an adjacent IrO_x catalyst particle (0.001125). The calculated efficiency QE is 0.17. It is assumed that only photolysis light absorbed by those ZrOCo units which are coupled to an Ir oxide nanocluster results in CO_2 reduction to CO. While we have no direct measurement to confirm this assumption, the total concentration of ZrOCo units of 1% (relative to Si) implies that the average spatial separation between the units is a too large for energy transfer to occur. Although most likely fortuitous, it is interesting to note that the QE of 17% is close to the value found previously for visible light induced water oxidation at $TiOCr^{III}$–IrO_x units (13%).[36] Ir oxide nanoclusters were of 2 nm size in this earlier study as well, although the fraction β of TiOCr units with an adjacent IrO_x catalyst particle was much higher (0.1), most probably because the spatially directed deposition of Ir precursor could be conducted by a spontaneous (dark) rather than a photoinduced redox process.[36] As a consequence, the external quantum efficiency, $2N_{CO}/N_{incident\_photons}$, was much higher for the TiOCr–IrO_x system (2.2×10^{-3}) than for the $ZrOCo^{II}$–IrO_x case reported here (1.3×10^{-5}).

The good photocatalytic quantum efficiency implies favorable competition of charge transfer from the excited ZrOCo unit to the Ir oxide catalyst cluster and to CO_2 molecules compared with back electron transfer within the light absorber. While monitoring of electron transfer of the excited $ZrOCo^{II}$ chromophore by transient optical absorption spectroscopy is rendered difficult by the intense and complex ligand field spectrum of Co in its II and III oxidation states, we have conducted such a study for the spectroscopically more amenable $TiOMn^{II}$ unit anchored on mesoscale channel surfaces of SBA-15 or a silica nanoparticle surface.[41,44] Observation of the ligand field absorption of transient Ti^{III} following MMCT excitation $Ti^{IV}OMn^{II} \rightarrow Ti^{III}OMn^{III}$ revealed a long lifetime for the excited MMCT state of 2.4 μs at room temperature (in vacuum). A low activation barrier and a very weak coupling of the electronic surfaces derived from a temperature dependent kinetic study suggest spin flip as the origin of the slow back electron transfer process.[44] The fact that most of the dozen or so heterobinuclear units investigated so far act as efficient charge transfer chromophores for driving redox reactions suggests that long (nano- or microsecond) lifetimes of the excited MMCT state are typical for these units. Because all units feature a transient Ti^{III} or Zr^{III} acceptor center upon MMCT excitation, spin flip of the Ti or Zr valence electron resulting in relaxation to a lower spin state is the most likely mechanism responsible for spin forbidden transition upon back electron transfer to high spin ground state. For the $ZrOCo^{II}$ unit, intersystem crossing from the S = 3/2 high spin excited $Zr^{III}OCo^{III}$ state (prepared by spin-allowed photoexcitation of the S = 3/2 ground state)[35] to the S = 1/2 low spin excited MMCT surface would result in a slow back electron transfer to ground state $Zr^{IV}OCo^{II}$. Therefore, hole transfer from transient Co^{III} in the S = 1/2 excited MMCT state to the IrO_x cluster is expected to be competitive with back electron transfer within the ZrOCo unit. Fast reduction of Co^{III} to Co^{II} by electron transfer from IrO_x would extend the lifetime of Zr^{III} and thereby facilitate electron transfer to CO_2. We conclude that slow back electron transfer of the excited $Zr^{III}OCo^{III}$ state is likely rendering hole transfer from Co to an adjacent IrO_x catalyst cluster competitive and considered to be the key factor responsible for the good quantum efficiency of CO_2 reduction by H_2O.

A quantum efficiency of 0.17 in light of a back electron transfer time of 1 μs would imply a charge (hole) transfer time from transient $Zr^{III}OCo^{III}$ to the IrO_x cluster of 6 μs. This is one to 2 orders of magnitude faster than previously reported hole transfer between a Ru bipyridine light absorber and IrO_x nanoparticle catalyst. For Ir oxide nanoparticles with anchored Ru bipyridine sensitizer, Mallouk observed a hole transfer time of 2.2 ms.[60] Introduction of a benzimidazole-phenol electron relay resulted in a substantial improvement of the transfer time by approximately a factor of 3.[1,61] On the other hand, for a Ru polyoxotungstate catalyst electrostatically attached to Ru bipyridine type chromophore, Hill et al.[4] and the groups of Bonchio and Scandola[5] reported very fast hole transfer of 1 ns. A critical common feature of the ZrOCo–IrO_x unit and the molecular light absorber–catalyst systems reported in the literature is the control of the spatial arrangement of the catalyst in proximity of the chromophore by chemical or photochemical methods. Regarding the photodeposition method, it was initially employed for attaching metal nanoparticle catalysts for hydrogen evolution to semiconductor surfaces.[62−64] Examples for the photodeposition of metal oxides as water oxidation catalysts on anodes include Co oxide on ZnO[65] or nanostructured Fe_2O_3.[66] Interestingly, facet selective photodeposition of noble metal and metal oxide clusters on TiO_2 crystals was observed by Ohno et al.[67] Very recently, facet selective photodeposition of metal oxide water oxidation and noble metal reduction catalysts particles was demonstrated for $BiVO_4$ crystals.[68] While the spatial relationship between the Co donor center and the IrO_x nanocluster after the calcination step cannot be evaluated based on the present spectroscopic results, our observation of photocatalytic function exclusively in the case of photodeposited clusters, but not for samples with randomly distributed Ir oxide clusters demonstrates that the photodeposition process is a necessary step for establishing charge transfer contact between ZrOCo unit and catalyst.

The mechanism of four-electron oxidation of water molecules at the IrO_x nanocluster features an IrOOH surface intermediate as detected in our recent rapid-scan ATR FT-IR study in aqueous solution.[53] The formation of the OO bond is proposed to occur by nucleophilic attack of H_2O on an $Ir^V{=}O$ species,[53] similar to water oxidation at Co_3O_4 nanoparticle surfaces where OO bond formation of $Co^{IV}{=}O$ moieties with H_2O molecules has been investigated by time-resolved FT-IR spectroscopy.[69] By contrast, no intermediate has thus far been reported for CO_2 reduction at a transient Zr^{III} center. The energetically most accessible intermediate of one-electron reduction of CO_2 is a HOCO radical (hydroxycarbonyl).[70] Because an adsorbed CO_2 molecule on the silica pore surface in the vicinity of a ZrOCo unit has a high probability of interacting by hydrogen bonding with one of the many SiOH groups ($2–3$ nm^{-2}),[71] it is reasonable to assume that formation of a HOCO intermediate is the first reduction step.

dx.doi.org/10.1021/ja504753g | J. Am. Chem. Soc. 2014, 136, 11034−11042

Dissociation of HOCO yields CO, which is known from time-resolved step-scan FT-IR studies to escape from the SBA-15 channels into the gas phase rapidly, with a time constant of 344 μs.[72] The fate of the departing OH radical is either disproportionation by reaction with another OH radical to form H_2O and O_2 or, more likely, adsorption on the IrO_x catalyst surface followed by oxidation to O_2. In this context, it is interesting to note that the fate of the departing O upon photoreduction of CO_2 to CO depends on the nature of the reagent, or catalyst, that delivers the electrons: For reduction of CO_2 to CO at $ZrOCu^{I}$ units, ^{18}O labeling of carbon dioxide directly demonstrated that the departing O of CO_2 ends up in a H_2O molecule.[32] If alkyl amine is used as sacrificial electron source like in our study of the MMCT induced CO_2 reduction half reaction of $ZrOCo^{II}$, the departing O is incorporated into the organic donor (in the case of triethylamine in the form of acetaldehyde product).[43] In the case of 266 nm O−Ti LMCT induced CO_2 reduction by H_2O at tetrahedral Ti centers inside mesoporous silica Ti-MCM-41 where no electrons from a donor or catalyst is available, disproportionation of OH radicals is the only accessible path.[27] Independent of the fate of the departing oxygen, in all cases of photochemical CO_2 splitting to CO in a mesoporous silica support including the $ZrOCo^{II}$–IrO_x case reported here, the rapid escape of CO from the mesoscale channels prevents back reaction from occurring.

The finding that for H_2O concentrations above 0.1 Torr the photochemical product yield decreases sharply is most likely due to coordination of the Zr site with water molecules, thus interfering with access of CO_2 molecules to transient Zr^{III}. The absence of a proton conducting membrane that separates not only emerging intermediates and final products, but also reactants from accessing the "wrong" catalytic site is a critical next step to address.

5. CONCLUSIONS

In summary, photodeposition of an Ir oxide nanocluster at a $ZrOCo^{II}$ binuclear unit under visible light excitation of the MMCT transition affords charge transfer coupling of the Ir oxide catalyst cluster with the Co donor center. The successful coupling of the Co donor center to the water oxidation catalyst is demonstrated by the observed CO_2 reduction to CO under evolution of O_2 when illuminating the photocatalytic unit exposed to a mixture of carbon dioxide and water vapor. The origin of the CO and O_2 products were confirmed by isotopic labeling of CO_2 and H_2O. This is the first observation of a closed photosynthetic cycle at an all-inorganic polynuclear cluster featuring a molecularly defined light absorber. Completion of the cycle implies a sufficiently short charge transfer time between Ir oxide cluster and transient Co^{III} center to compete successfully with $Zr^{III}OCo^{III} \rightarrow Zr^{IV}OCo^{II}$ back electron transfer. The reduced $Zr^{III}OCo^{II}$ state so formed renders the lifetime of the electron on the Zr center sufficiently long for activation of CO_2 to occur, resulting in the splitting to CO. Instant escape of the CO and O_2 products from the silica pores effectively prevents back reaction.

As a single photon light absorber for driving the conversion of CO_2 to CO and O_2 with its 62 kcal mol^{-1} free energy of reaction, the $ZrOCo$–IrO_x system is limited to extreme blue and near UV region despite the fact that the MMCT chromophore absorbs light up to 550 nm. Therefore, coupling of two heterobinuclear units in a two-photon scheme, one for driving the CO_2 reduction and one coupled to a H_2O oxidation catalyst, is an important next step for enabling the use of photons across the visible region. Furthermore, separation of water oxidation catalysis from the carbon dioxide reduction chemistry by a proton conducting, gas impermeable membrane is essential to minimize back reaction and prevent access of reactants and intermediates to the wrong catalytic sites. The development of nanoscale assemblies with these properties is in progress in our lab.

■ ASSOCIATED CONTENT

Supporting Information

Spectroscopic data for characterization (XRD, UV−vis, FT-IR, and XPS), and control experiments for photochemical CO_2 reduction. This material is available free of charge via the Internet at http://pubs.acs.org

■ AUTHOR INFORMATION

Corresponding Author

HMFrei@lbl.gov

Notes

The authors declare no competing financial interest.

■ ACKNOWLEDGMENTS

This work was supported by the Director, Office of Science, Office of Basic Energy Sciences, Division of Chemical, Geological and Biosciences of the U.S. Department of Energy under Contract No. DE-AC02-05CH11231. The authors acknowledge the support of the National Center for Electron Microscopy, Lawrence Berkeley National Laboratory, which is supported by the U.S. Department of Energy. W.K. thankful for support from the Basic Science Research Program through the National Research Foundation of Korea (NRF) funded by the Ministry of Education (2012R1A6A3A03039210). The authors thank Drs. Diana Cedeno and Wenjun Liu, Joint Center for Artificial Photosynthesis at LBNL, for conducting XPS and NMR measurements.

■ REFERENCES

(1) Zhao, Y.; Swierk, J. R.; Megiatto, J. D.; Sherman, B.; Youngblood, W. J.; Qin, D.; Lentz, D. M.; Moore, A. L.; Moore, T. A.; Gust, D.; Mallouk, T. E. *Proc. Natl. Acad. Sci. U.S.A.* **2012**, *109*, 15612−15616.
(2) Brimblecombe, R.; Koo, A.; Dismukes, G. C.; Swiegers, G. F.; Spiccia, L. *J. Am. Chem. Soc.* **2010**, *132*, 2892−2894.
(3) Li, L.; Duan, L.; Xu, Y.; Gorlov, M.; Hagfeldt, A.; Sun, L. *Chem. Commun.* **2010**, *46*, 7307−7309.
(4) Xiang, X.; Fielden, J.; Rodriguez-Cordoba, W.; Huang, Z.; Zhang, N.; Luo, Z.; Musaev, D. G.; Lian, T.; Hill, C. L. *J. Phys. Chem. C* **2013**, *117*, 918−926.
(5) Orlandi, M.; Argazzi, R.; Sartorel, A.; Carraro, M.; Scorrano, G.; Bonchio, M.; Scandola, F. *Chem. Commun.* **2010**, *46*, 3152−3154.
(6) Song, W.; Glasson, C. R. K.; Luo, H.; Hanson, K.; Brennaman, M. K.; Concepcion, J. J.; Meyer, T. J. *J. Phys. Chem. Lett.* **2011**, *2*, 1808−1813.
(7) Vagnini, M. T.; Smeigh, A. L.; Blakemore, J. D.; Eaton, S. W.; Schley, N. D.; D'Souza, F.; Crabtree, R. H.; Brudvig, G. W.; Dick, D. T.; Wasielewski, M. R. *Proc. Natl. Acad. Sci. U.S.A.* **2012**, *109*, 15651−15656.
(8) Koike, K.; Naito, S.; Sato, S.; Tamaki, Y.; Ishitani, O. *J. Photochem. Photobiol., A* **2009**, *207*, 109−114.
(9) Bian, Z. Y.; Chi, S. M.; Li, L.; Fu, W. *Dalton Trans.* **2010**, *39*, 7884−7887.
(10) Schneider, J.; Vuong, K. Q.; Calladine, J. A.; Sun, X. Z.; Whitwood, A. C.; George, M. W.; Perutz, R. N. *Inorg. Chem.* **2011**, *50*, 11877−11889.

(11) Kiyosawa, K.; Shiraishi, N.; Shimada, T.; Masui, D.; Tachibana, H.; Takagi, S.; Ishitani, O.; Tryk, D. A.; Inoue, H. *J. Phys. Chem. C* **2009**, *113*, 11667−11673.
(12) Sato, S.; Morikawa, T.; Saeki, S.; Kajino, T.; Motohiro, T. *Angew. Chem., Int. Ed.* **2010**, *49*, 5101−5105.
(13) Rocheleau, R. E.; Miller, E. L.; Misra, A. *Energy Fuels* **1998**, *12*, 3−10.
(14) Reece, S. Y.; Hamel, J. A.; Sung, K.; Jarvi, T. D.; Esswein, A. J.; Pijpers, J. J. H.; Nocera, D. G. *Science* **2011**, *334*, 645−648.
(15) Khaselev, O.; Turner, J. A. *Science* **1998**, *280*, 425−427.
(16) Brillet, J.; Yum, J. H.; Cornuz, M.; Hisatomi, T.; Solarska, R.; Augustynski, J.; Gratzel, M.; Sivula, K. *Nat. Photonics* **2012**, *6*, 824−828.
(17) Abdi, F. F.; Han, L.; Smets, A. H. M.; Zeman, M.; Dam, B.; van de Krol, R. *Nature Commun.* **2013**, *4*, 1−7.
(18) Liu, C.; Tang, J.; Chen, H. M.; Liu, B.; Yang, P. *Nano Lett.* **2013**, *13*, 2989−2992.
(19) Shaner, M. R.; Fountaine, K. T.; Ardo, S.; Coridan, R. H.; Atwater, H. A.; Lewis, N. *Energy Environ. Sci.* **2014**, *7*, 779−790.
(20) Maeda, K.; Teramura, K.; Lu, D.; Takata, T.; Saito, N.; Inoue, Y.; Domen, K. *Nature* **2006**, *440*, 295.
(21) Hemminger, J. C.; Carr, R.; Somorjai, G. A. *Chem. Phys. Lett.* **1978**, *57*, 100−104.
(22) Inoue, T.; Fujishima, A.; Konishi, S.; Honda, K. *Nature* **1979**, *277*, 637−638.
(23) Sayama, K.; Arakawa, H. *J. Phys. Chem.* **1993**, *97*, 531−533.
(24) Iizuka, K.; Wato, T.; Miseki, Y.; Saito, K.; Kudo, A. *J. Am. Chem. Soc.* **2011**, *133*, 20863−20868.
(25) Anpo, M.; Yamashita, H.; Ikeue, K.; Fujii, Y.; Zhang, S. G.; Ichihashi, Y.; Park, D. R.; Suzuki, Y.; Koyano, K.; Tatsumi, T. *Catal. Today* **1998**, *44*, 327−332.
(26) Anpo, M.; Takeuchi, M. *J. Catal.* **2003**, *216*, 505−516.
(27) Lin, W.; Han, H.; Frei, H. *J. Phys. Chem. B* **2004**, *108*, 18269−18273.
(28) Yang, C. C.; Yu, Y. H.; v. d. Linden, B.; Wu, J. C. S.; Mul, G. *J. Am. Chem. Soc.* **2010**, *132*, 8398−8406.
(29) Sato, S.; Arai, T.; Morikawa, T.; Uemura, K.; Suzuki, T. M.; Tanaka, H.; Kajino, T. *J. Am. Chem. Soc.* **2011**, *133*, 15240−15243.
(30) Xie, S.; Wang, Y.; Zhang, Q.; Fan, W.; Deng, W.; Wang, Y. *Chem. Commun.* **2013**, *49*, 2451−2453.
(31) Kim, W.; Seok, T.; Choi, W. *Energy Environ. Sci.* **2012**, *5*, 6066−6070.
(32) Lin, W.; Frei, H. *J. Am. Chem. Soc.* **2005**, *127*, 1610−1611.
(33) Lin, W.; Frei, H. *J. Phys. Chem. B* **2005**, *109*, 4929−4935.
(34) Han, H.; Frei, H. *Microporous Mesoporous Mater.* **2007**, *103*, 265−272.
(35) Han, H.; Frei, H. *J. Phys. Chem. C* **2008**, *112*, 8391−8399.
(36) Han, H.; Frei, H. *J. Phys. Chem. C* **2008**, *112*, 16156−16159.
(37) Okamoto, A.; Nakamura, R.; Osawa, H.; Hashimoto, K. *Langmuir* **2008**, *24*, 7011−7017.
(38) Okamoto, A.; Nakamura, R.; Osawa, H.; Hashimoto, K. *J. Phys. Chem. C* **2008**, *112*, 19777−19783.
(39) Wu, X.; Weare, W. W.; Frei, H. *Dalton Trans.* **2009**, 10114−10121.
(40) Frei, H. *Chimia* **2009**, *63*, 721−730.
(41) Cuk, T.; Weare, W. W.; Frei, H. *J. Phys. Chem. C* **2010**, *114*, 9167−9172.
(42) Soo, H. S.; Macnaughtan, M. L.; Weare, W. W.; Yano, J.; Frei, H. *J. Phys. Chem. C* **2011**, *115*, 24893−24905.
(43) Macnaughtan, M. L.; Soo, H. S.; Frei, H. *J. Phys. Chem. C* **2014**, *118*, 7874−7885.
(44) McClure, B. A.; Frei, H. *J. Phys. Chem. C* **2014**, *118*, 11601−11611.
(45) Isakova, V. G.; Baidina, I. A.; Morozova, N. B.; Igumenov, I. K. *Polyhedron* **2000**, *19*, 1097−1103.
(46) Brown, A. J.; Howarth, O. W.; Moore, P. *J. Am. Chem. Soc.* **1978**, *100*, 713−717.
(47) Kang, K. K.; Ahn, W. S. *J. Mol. Catal. A: Chem.* **2000**, *159*, 403−410.
(48) Maschmeyer, T.; Rey, F.; Sankar, G.; Thomas, J. M. *Nature* **1995**, *378*, 159−162.
(49) Baur, J. E.; Spaine, T. W. *J. Electroanal. Chem.* **1998**, *443*, 208−216.
(50) Zhao, Y.; Hernandez-Pagan, E. A.; Vargas-Barbosa, N. M.; Dysart, J. L.; Mallouk, T. E. *J. Phys. Chem. Lett.* **2011**, *2*, 402−406.
(51) Nagashima, N.; Kudoh, S.; Takayanagi, M.; Nakata, M. *J. Phys. Chem. A* **2001**, *105*, 10832−10838.
(52) Greenwood, N. N.; Earnshaw, A. *Chemistry of the Elements*, 2nd ed.; Elsevier: Oxford, 1997.
(53) Sivasankar, N.; Weare, W. W.; Frei, H. *J. Am. Chem. Soc.* **2011**, *133*, 12976−12979.
(54) Morris, N. D.; Suzuki, M.; Mallouk, T. E. *J. Phys. Chem. A* **2004**, *108*, 9115−9119.
(55) Jiao, F.; Frei, H. *Angew. Chem., Int. Ed.* **2009**, *48*, 1841−1844.
(56) Nakagawa, T.; Beasley, C. A.; Murray, R. W. *J. Phys. Chem. C* **2009**, *113*, 12958−12961.
(57) Nakagawa, T.; Bjorge, N. S.; Murray, R. W. *J. Am. Chem. Soc.* **2009**, *131*, 15578−15579.
(58) Smith, R. D. L.; Sporinova, B.; Fagan, R. D.; Trudel, S.; Berlinguette, C. P. *Chem. Mater.* **2014**, *26*, 1654−1659.
(59) Stull, D. R.; Prophet, H. *JANAF Thermochemical Tables*, 2nd ed.; Natl. Stand. Ref. Data Ser.; National Bureau of Standards (U.S.): Washington, D.C, 1971; Vol *37*, p1.
(60) Youngblood, W. J.; Lee, S. H. A.; Kobayashi, Y.; Hernandez-Pagan, E. A.; Hoertz, P. G.; Moore, T. A.; Moore, A. L.; Gust, D.; Mallouk, T. E. *J. Am. Chem. Soc.* **2009**, *131*, 926−927.
(61) Swierk, J. R.; Mallouk, T. E. *Chem. Soc. Rev.* **2013**, *42*, 2357−2387.
(62) Kraeutler, B.; Bard, A. J. *J. Am. Chem. Soc.* **1978**, *100*, 4317−4318.
(63) Yoshida, M.; Yamakata, A.; Takanabe, K.; Kubota, J.; Osawa, M.; Domen, K. *J. Am. Chem. Soc.* **2009**, *131*, 13218−13219.
(64) Subramanian, V.; Wolf, E. E.; Kamat, P. V. *J. Am. Chem. Soc.* **2004**, *126*, 4943−4950.
(65) Steinmiller, E. M. P.; Choi, K.-S. *Proc. Natl. Acad. Sci. U.S.A.* **2009**, *106*, 20633−20636.
(66) Zhong, D. K.; Cornuz, M.; Sivula, K.; Gratzel, M.; Gamelin, D. R. *Energy Environ. Sci.* **2011**, *4*, 1759−1764.
(67) Ohno, T.; Sarukawa, K.; Matsumura, M. *New J. Chem.* **2002**, *26*, 1167−1170.
(68) Li, R.; Han, H.; Zhang, F.; Wang, D.; Li, C. *Energy Environ. Sci.* **2014**, *7*, 1369−1376.
(69) Zhang, M.; De Respinis, M.; Frei, H. *Nat. Chem.* **2014**, *6*, 362−367.
(70) Ulagappan, N.; Frei, H. *J. Phys. Chem. A* **2000**, *104*, 7834−7839.
(71) Zhao, X. S.; Lu, G. Q.; Whittaker, A. K.; Millar, G. J.; Zhu, H. Y. *J. Phys. Chem. B* **1997**, *101*, 6525−6531.
(72) Anderson, L. K.; Frei, H. *J. Phys. Chem. B* **2006**, *110*, 22601−22607.